



Five-dimensional visualization of phase transition in BiNiO₃ under high pressure

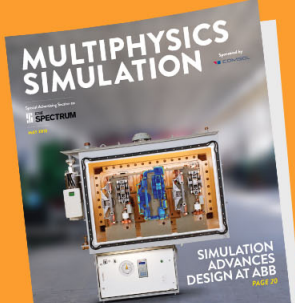
Yijin Liu, Junyue Wang, Masaki Azuma, Wendy L. Mao, and Wenge Yang

Citation: [Applied Physics Letters](#) **104**, 043108 (2014); doi: 10.1063/1.4863229

View online: <http://dx.doi.org/10.1063/1.4863229>

View Table of Contents: <http://scitation.aip.org/content/aip/journal/apl/104/4?ver=pdfcov>

Published by the [AIP Publishing](#)



The cover of the 'Multiphysics Simulation' e-magazine features a photograph of a complex electronic circuit board. The text on the cover includes 'MULTIPHYSICS SIMULATION' at the top, 'SPECTRUM' in a small box, and 'SIMULATION ADVANCES DESIGN AT ABB' at the bottom right.

FREE Multiphysics Simulation e-Magazine

[DOWNLOAD TODAY >>](#)

 COMSOL

Five-dimensional visualization of phase transition in BiNiO₃ under high pressure

Yijin Liu,^{1,a)} Junyue Wang,^{2,3} Masaki Azuma,⁴ Wendy L. Mao,^{5,6,7} and Wenge Yang^{2,3,a)}

¹Stanford Synchrotron Radiation Lightsource, SLAC National Accelerator Laboratory, 2575 Sand Hill Road, Menlo Park, California 94025, USA

²Center of High Pressure Science and Technology Advanced Research (HPSTAR), Shanghai 201203, People's Republic of China

³High Pressure Synergetic Consortium, Geophysical Laboratory, Carnegie Institution of Washington, 9700 S Cass Avenue, Argonne, Illinois 60439, USA

⁴Materials and Structures Laboratory, Tokyo Institute of Technology, 4259 Nagatsuta, Yokohama 226-8503, Japan

⁵Geological and Environmental Sciences, 450 Serra Mall, Stanford University, Stanford, California 94305, USA

⁶SLAC National Accelerator Laboratory, Stanford Institute for Materials and Energy Sciences, 2575 Sand Hill Road, Menlo Park, California 94025, USA

⁷Photon Science, SLAC National Accelerator Laboratory, 2575 Sand Hill Road, Menlo Park, California 94025, USA

(Received 21 November 2013; accepted 31 December 2013; published online 29 January 2014)

Colossal negative thermal expansion was recently discovered in BiNiO₃ associated with a low density to high density phase transition under high pressure. The varying proportion of co-existing phases plays a key role in the macroscopic behavior of this material. Here, we utilize a recently developed X-ray Absorption Near Edge Spectroscopy Tomography method and resolve the mixture of high/low pressure phases as a function of pressure at tens of nanometer resolution taking advantage of the charge transfer during the transition. This five-dimensional (X, Y, Z, energy, and pressure) visualization of the phase boundary provides a high resolution method to study the interface dynamics of high/low pressure phase. © 2014 AIP Publishing LLC. [<http://dx.doi.org/10.1063/1.4863229>]

BiNiO₃ undergoes a phase transition induced by external pressure or temperature accompanying by the intermetallic charge transfer between Bi and Ni ions. The observation of colossal negative thermal expansion at extended pressure and temperature range makes this transition of great potential in functional material design.¹ Different techniques, such as X-ray diffraction (XRD), neutron diffraction (ND), and X-ray absorption spectroscopy (XAS), have been applied to study the bulk property of this material.^{2,3} The varying proportion of co-existing phases plays a key role in controlling the overall behavior of the material over the transition pressure/temperature range. To understand the micro-mechanism and improve the property, it is crucial to investigate the phase distribution in a three dimensional (3D) spatially resolved manner (i.e., with high resolution 3D imaging techniques) to help elucidate the underlying chemistry and physics behind the measured properties.

There are many advanced microscopy techniques with nanoscale capabilities available via optical/electron probes. However, most of these nanoscale techniques require either contact mode or vacuum conditions, and suffer from the limitation of penetration depth, which is essential for *in-situ* studies of the material. In this work, we employed the transmission X-ray microscopy (TXM) technique⁴⁻¹⁰ to investigate the sample under *in-situ* environments, i.e., high external pressure. TXM provides the capability of 3D imaging at high spatial resolution¹¹ (~30 nm in all three

directions) over a field of view of about 30 × 30 × 30 μm³. Combined with the energy tunability of incident X-rays from a synchrotron source, the chemical species and/or valence state of materials can be distinguished¹²⁻¹⁵ via performing a X-ray Absorption Near Edge Spectrum (XANES) style 3D tomography study on a specific element of interest in a reasonable time frame (i.e., a few hours).¹³

In this study, we adopted a specially designed diamond anvil cell (DAC) for enlarging the accessible viewing angle in the tomography scan and the TXM capabilities to enable the *in-situ* morphology study of a ~10-μm-sized BiNiO₃ particle (see Fig. 1). By tuning the incident x-ray energy across the Ni absorption edge, we were able to observe charge transfer induced changes in the spectroscopic data in both the bulk XANES measurements and the TXM measurements. We present here the detailed high pressure phase (HPP) to low pressure phase (LPP) boundary *in-situ* detection at multiple pressure points at which both phases coexisted. The quantitative measurements of the ratio of high pressure to low pressure phase and the phase boundary allow us to directly visualize the phase volume and shape evolution under pressure. This five-dimensional (X, Y, Z, energy, and pressure) visualization of the phase transition also provides important insight into the mechanism of the pressure induced phase growth.

We adapt the combination of the full field X-ray imaging technique and X-ray spectroscopy for the microstructure study of materials under *in-situ* high pressure environment. In this technological development, a 2D area detector is coupled with an X-ray energy scan, which results in the collection of an X-ray absorption spectrum at each pixel at tens of nm spatial

^{a)}Authors to whom correspondence should be addressed. Electronic addresses: liuyijin@slac.stanford.edu and wyang@ciw.edu.

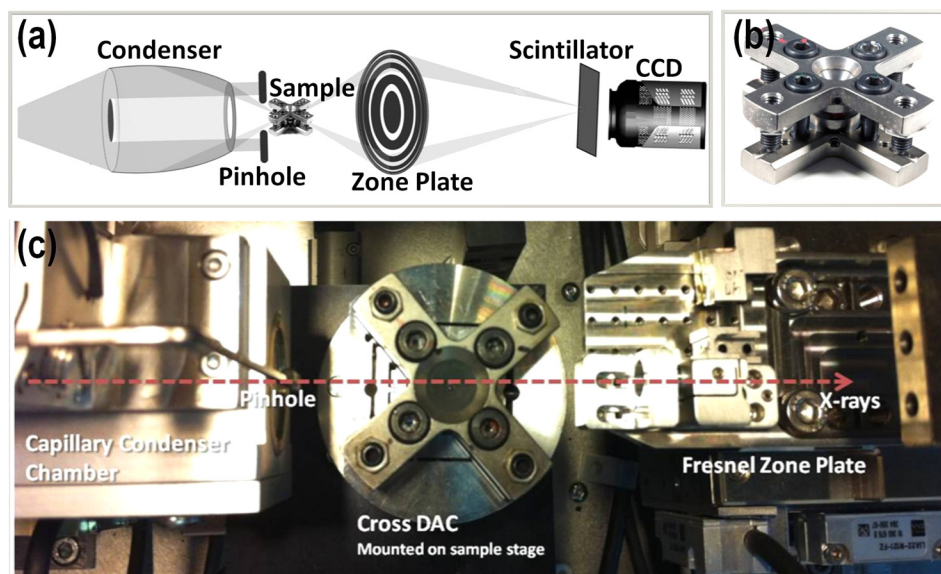


FIG. 1. (a) Schematic drawing of the transmission X-ray microscope installed at beamline 6-2C of SSRL. (b) Specially designed X-DAC for 3D tomography study. (c) Top view of the TXM system with the XDAC mounted on the sample stage.

resolution in the TXM setup (over a time period of 10 to 20 min for 2D XANES imaging). Another way to look at this development is that the use of an area detector in spectroscopy measurement is equivalent to the collection of spectroscopic data with millions of “pixel detectors” working simultaneously (typically, $2k \times 2k$ pixels for commercially available detectors). It becomes more useful when tomography is also conducted at each energy point. The capability of spatially resolving the distribution of different chemical species in 3D now opens enormous opportunities in a myriad of *in-situ* materials study at various working environments.^{16–20}

The schematic of the transmission X-ray microscope installed at beamline 6-2C of the Stanford Synchrotron Radiation Lightsource (SSRL) of SLAC National Accelerator Laboratory is shown in Fig. 1(a). The detailed specifications of this microscope have been described previously.²¹ A specially designed cross-DAC (X-DAC, see Fig. 1(b)) for the TXM system was used as the *in-situ* high pressure vessel. A beryllium gasket was pre-indented to $40 \mu\text{m}$ thick and a hole with a $120 \mu\text{m}$ diameter was drilled in the center to serve as the sample chamber. Silicone oil was used as pressure transmitting medium (PTM) to create a quasi-hydrostatic pressure environment for the sample, and a ruby ball was loaded in the sample chamber for pressure calibration.²² In this experiment, tomography of the investigated BiNiO_3 particle was performed at twenty selected X-ray energies across the near absorption K-edge of nickel element over an angular range opening of 135° with 1° increments to identify the chemical species present within each $30 \times 30 \times 30 \text{ nm}^3$ voxel. For minimizing the effect from the missing viewing angles due to the use of supporting screws, an iterative tomography reconstruction algorithm was adopted.²³ Automatic image registration and reconstruction were performed using the TXM-Wizard software package.²⁴

The polycrystalline sample BiNiO_3 was synthesized at high-pressure and temperature.²⁵ *In-situ* high pressure powder XRD shows the pressure range of the co-existence of both high and low pressure phases is about 3–5 GPa. We selected three different pressures at 3.89, 4.17, and 4.55 GPa in this work to perform the XANES type tomography across Ni K-edge. Twenty of the 3D matrices are reconstructed from the energy dependent tomography dataset (see Fig.

2(a)). As one follows the change of the reconstructed absorption coefficient over every single voxel as a function of the X-ray energy, “voxel spectra” can be extracted (see Fig. 2(b)). The characteristic features of these voxel spectra are finger prints of the chemical species and valence states, and can be used to determine the relative molar ratio of two phases within the corresponding voxel by performing linear combination fitting to the pure low pressure and high pressure spectra. Fig. 2(c) shows both pure low pressure and high pressure XANES spectra collected from bulk sample at an XAFS beamline 20BM-B at the Advanced Photon Source (APS) of Argonne National Laboratory (ANL). The most significant difference in spectra between the LPP and the HPP is the white line height. By interpolating the portion of HPP/LPP at each voxel, the 3D distribution of the LPP and HPP are retrieved and rendered in Fig. 2(d).

The energy resolved 3D TXM imaging was conducted at three different pressures (3.89, 4.17, and 4.55 GPa). Iterative tomography reconstructions generated the 3D distributions of the absorption coefficient at twenty discrete energies across the near edge absorption range allowing us to plot the spectrum for every single voxel showing both its energy dependence and its chemical fingerprint. Standard spectrum normalization and linear combination fitting¹³ was performed for every single voxel through the entire volume resolving the HPP/LPP ratio over the corresponding voxels. The 3D map of edge jump (defined here, as the difference between the 3D matrices of absorption coefficient at the highest and the lowest energies) gives us the distribution of the Ni concentration, which is then divided into two parts, the HPP and the LPP, based on the percentage retrieved from the spectrum fitting. In Fig. 3, we present the 3D isosurface renderings of both the LPP and the HPP portions at three pressures. As one can see clearly, the HPP portions start from isolated locations and evolve into connected volumes. Two LPP regions highlighted by circles persisted to highest pressure studied.

To present the detail phase boundary structure, 2D slices through a selected depth of the 3D volumes are displayed in Fig. 4. The HPP portion was largely initiated from many small regions at different locations. As the pressure

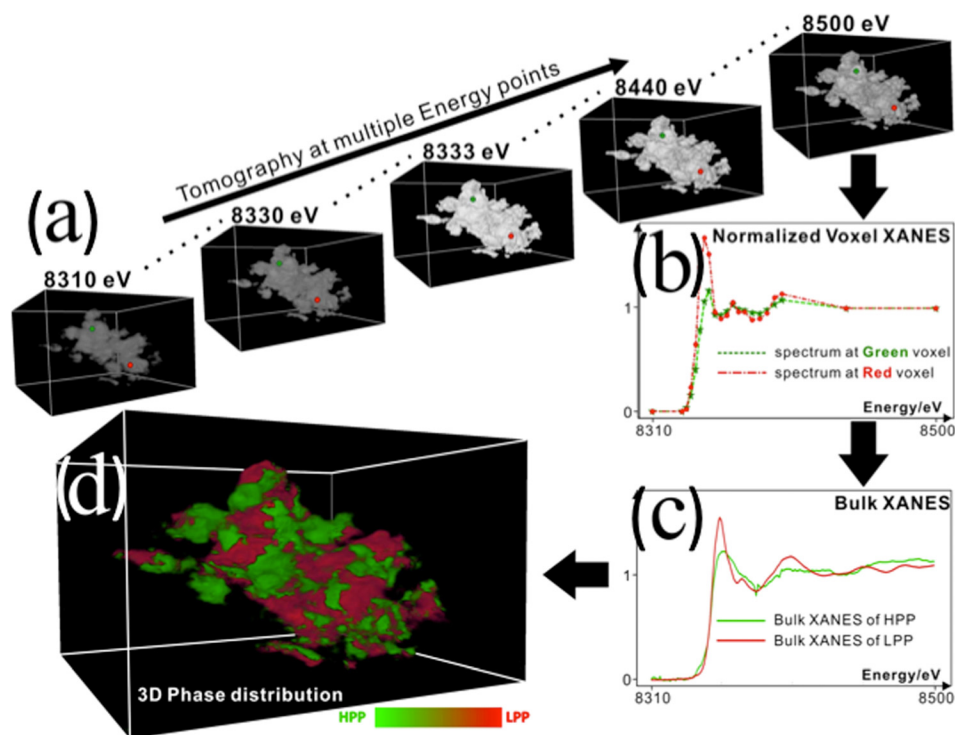


FIG. 2. (a) Reconstructed 3D volumes of the investigated particle at multiple X-ray energies. (b) Intensity plots of two selected voxels (highlighted in panel (a)) as a function of the photon energy. By performing linear combination fitting of each voxel XANES to the standard spectra of the low pressure phase and the high pressure phase (panel (c), acquired using bulk spectroscopy technique), the distribution of the phases are resolved and rendered in panel (d) (color coded as defined by the color map).

increases, the isolated HPP parts grow larger, merge together, and eventually become connected. In the middle row of Fig. 4, the HPP pixels were binarized and displayed. The arrows point to the locations where the HPP evolves from isolated islands to connected regions, while the dashed white circle indicates a portion where many isolated fragments merged into a solid HPP grain.

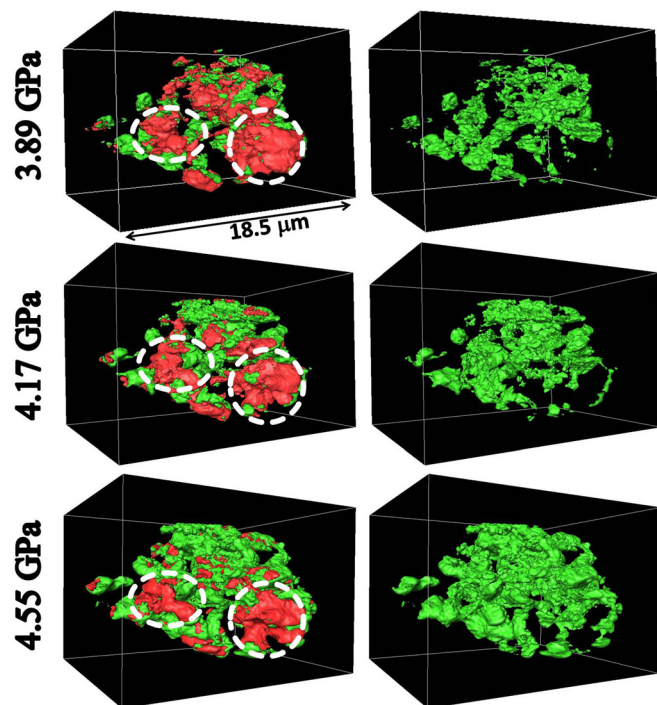


FIG. 3. LPP (red) and HPP (green) portions of the BiNiO_3 particle as a function of pressure. The left column shows both the LPP and HPP, with the scale bar on the top panel. The right column shows only the portion of HPP. The circled regions in the left column indicate the local atoms that remain LPP to the highest pressure 4.55 GPa in this study.

The above characteristic features of HPP distribution are analogous to nucleation and grain growth that occurs upon heating. Usually, nucleation starts from many seed locations like the initial HPP distribution. Upon heating, the local curvature of the grain boundary drives the grain growth to reduce the total amount of grain boundary surface, i.e., interfacial energy of the system.²⁶ Under high pressure, the HPP is thermodynamically stable, i.e., lower energy phase. There is therefore a driving force to switch from the LPP atomic structure to the HPP one. We expect the LPP/HPP interfacial areas are the favored location. The Canny edge detection algorithm²⁷ was applied to each slice through different depth of the 3D matrices. As demonstrated in the bottom row of Fig. 4, the HPP/PTM interface, the LPP/PTM interface and the HPP/LPP boundary can be clearly detected.

It worth emphasizing that the results presented here represent a five dimensional (X, Y, Z, energy, and pressure) visualization of the phase transition, which shows the change of chemically resolved morphology as a function of pressure.

As the starting particle is in the form of a powder, the phase transition can start from any grain. The inhomogeneity in the distribution of the high pressure phase demonstrates the internal pressure fluctuation inside the particle. The detail shape of phase boundary provides the driving force for the phase boundary movement, which can give guidance for developing a pressure induced phase growth mechanism and boundary dynamics.

In this study, we developed a powerful imaging technique on the pressure induced phase transition in a five dimensional manner (X, Y, Z, energy, and pressure) at a spatial resolution of ~ 30 nm in 3D. The quantitative results (including the volume measurement and the phase boundary shape detection) of the distribution of different phases provide important insight into the underlying mechanism, which is otherwise unavailable.

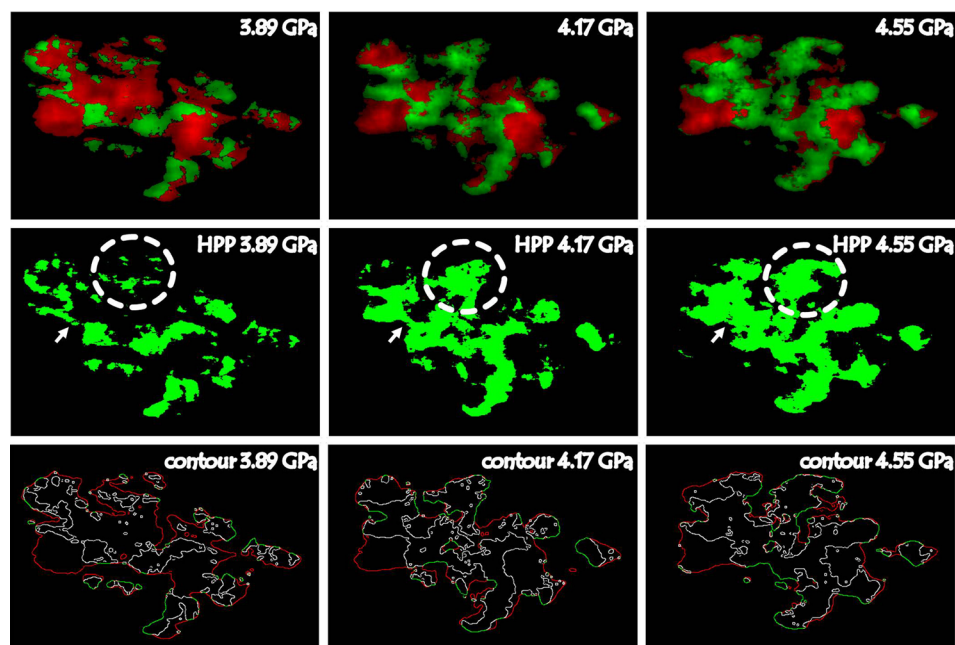


FIG. 4. Detail view of a single 2D slice at three different pressures. Top shows the images of LPP (red) and HPP (green) together with the brightness reflecting the Ni concentration. Middle row shows HPP only. Dashed white circle in the middle row shows the growth of isolated islands into a large piece; the arrow points to a location where separated pieces become connected. The bottom row shows the phase boundaries (LPP to HPP (white line), LPP at sample edge (red line), and HPP at sample edge (green line)).

The authors gratefully thank Dr. Piero Pianetta and Dr. Joy C. Andrews for valuable discussions. HPSynC is supported as part of EFree, an Energy Frontier Research Center funded by DOE-BES under Grant No. DE-SC 0001057. The TXM at SSRL has been supported by NIH/NIBIB under Grant No. 5R01EB004321. SSRL is supported by the DOE-BES. Portions of the work were performed at HPCAT 16BM-D, and PNC/XSD 20BM-B, APS, ANL. HPCAT operations are supported by DOE-NNSA under Award No. DE-NA0001974 and DOE-BES under Award No. DE-FG02-99ER45775, with partial instrumentation funding by NSF. PNC/XSD facilities are supported by the US DOE-BES, a Major Resources Support grant from NSERC, the University of Washington, the Canadian Light Source and the Advanced Photon Source. APS is supported by DOE-BES, under Contract No. DE-AC02-06CH11357.

- ¹M. Azuma, W. Chen, H. Seki, M. Czapski, S. Olga, K. Oka, M. Mizumaki, T. Watanuki, N. Ishimatsu, N. Kawamura, S. Ishiwata, M. G. Tucker, Y. Shimakawa, and J. P. Attfield, *Nat. Commun.* **2**, 347 (2011).
- ²S. Ishiwata, M. Azuma, M. Hanawa, Y. Moritomo, Y. Ohishi, K. Kato, M. Takata, E. Nishibori, M. Sakata, I. Terasaki, and M. Takano, *Phys. Rev. B* **72**, 045104 (2005).
- ³M. Mizumaki, N. Ishimatsu, N. Kawamura, M. Azuma, Y. Shimakawa, M. Takano, and T. Uozumi, *Phys. Rev. B* **80**, 233104 (2009).
- ⁴U. Neuhausler, G. Schneider, W. Ludwig, M. A. Meyer, E. Zschech, and D. Hambach, *J. Phys. D: Appl. Phys.* **36**, A79 (2003).
- ⁵G.-C. Yin, M.-T. Tang, Y.-F. Song, F.-R. Chen, K. S. Liang, F. W. Duerwer, W. Yun, C.-H. Ko, and H.-P. D. Shieh, *Appl. Phys. Lett.* **88**, 241115 (2006).
- ⁶Y. S. Chu, J. M. Yi, F. De Carlo, Q. Shen, W.-K. Lee, H. J. Wu, C. L. Wang, J. Y. Wang, C. J. Liu, C. H. Wang, S. R. Wu, C. C. Chien, Y. Hwu, A. Tkachuk, W. Yun, M. Feser, K. S. Liang, C. S. Yang, J. H. Je, and G. Margaritondo, *Appl. Phys. Lett.* **92**, 103119 (2008).
- ⁷G. B. Kim, Y. J. Yoon, T. J. Shin, H. S. Youn, Y. S. Gho, and S. J. Lee, *Microsc. Res. Tech.* **71**, 639 (2008).
- ⁸W. Li, N. Wang, J. Chen, G. Liu, Z. Pan, Y. Guan, Y. Yang, W. Wu, J. Tian, S. Wei, Z. Wu, Y. Tian, and L. Guo, *Appl. Phys. Lett.* **95**, 053108 (2009).

- ⁹J. Wang, Y.-C. K. Chen, Q. Yuan, A. Tkachuk, C. Erdonmez, B. Hornberger, and M. Feser, *Appl. Phys. Lett.* **100**, 143107 (2012).
- ¹⁰T. L. Kao, C. Y. Shi, J. Wang, W. L. Mao, Y. Liu, and W. Yang, *Microsc. Res. Tech.* **76**(11), 1112 (2013).
- ¹¹Y. Liu, J. C. Andrews, J. Wang, F. Meirer, P. Zhu, Z. Wu, and P. Pianetta, *Opt. Express* **19**, 540 (2011).
- ¹²C. Rau, A. Somogyi, and A. Simionovici, *Nucl. Instrum. Methods Phys. Res., Sect. B* **200**, 444 (2003).
- ¹³F. Meirer, J. Cabana, Y. Liu, A. Mehta, J. C. Andrews, and P. Pianetta, *J. Synchrotron Radiat.* **18**, 773 (2011).
- ¹⁴G. J. Nelson, W. M. Harris, J. R. Izzo, Jr., K. N. Grew, W. K. S. Chiu, Y. S. Chu, J. Yi, J. C. Andrews, Y. Liu, and P. Pianetta, *Appl. Phys. Lett.* **98**, 173109 (2011).
- ¹⁵P. Guttman, C. Bittencourt, S. Rehbein, P. Umek, X. Ke, G. van Tendeloo, C. P. Ewels, and G. Schneider, *Nat. Photonics* **6**, 25 (2012).
- ¹⁶I. D. Gonzalez-Jimenez, K. Cats, T. Davidian, M. Ruitenbeek, F. Meirer, Y. Liu, J. Nelson, J. C. Andrews, P. Pianetta, F. M. F. de Groot, and B. M. Weckhuysen, *Angew. Chem.* **124**, 12152 (2012).
- ¹⁷U. Boesenberg, F. Meirer, Y. Liu, A. K. Shukla, R. Dell'Anna, T. Tyliczszak, G. Chen, J. C. Andrews, T. J. Richardson, R. Kostecki, and J. Cabana, *Chem. Mater.* **25**, 1664 (2013).
- ¹⁸K. H. Cats, I. D. Gonzalez-Jimenez, Y. Liu, J. Nelson, D. van Campen, F. Meirer, A. M. J. van der Eerden, F. M. F. de Groot, J. C. Andrews, and B. M. Weckhuysen, *Chem. Commun.* **49**, 4622 (2013).
- ¹⁹Y. Liu, F. Meirer, J. Wang, G. Requena, P. Williams, J. Nelson, A. Mehta, J. C. Andrews, and P. Pianetta, *Anal. Bioanal. Chem.* **404**, 1297 (2012).
- ²⁰J. Wang, Y. K. Chen-Wiegart, and J. Wang, *Chem. Commun.* **49**, 6480 (2013).
- ²¹J. C. Andrews, E. Almeida, M. C. van der Meulen, J. S. Alwood, C. Lee, Y. Liu, J. Chen, F. Meirer, M. Feser, J. Gelb, J. Rudati, A. Tkachuk, W. Yun, and P. Pianetta, *Microsc. Microanal.* **16**, 327 (2010).
- ²²H. K. Mao, J. Xu, and P. M. Bell, *J. Geophys. Res.* **91**, 4673, doi:10.1029/JB091iB05p04673 (1986).
- ²³J. Wang, W. Yang, S. Wang, X. Xiao, F. De Carlo, Y. Liu, and W. L. Mao, *J. Appl. Phys.* **111**, 112626 (2012).
- ²⁴Y. Liu, F. Meirer, P. A. Williams, J. Wang, J. C. Andrews, and P. Pianetta, *J. Synchrotron Radiat.* **19**, 281 (2012).
- ²⁵S. Ishiwata, M. Azuma, M. Takano, E. Nishibori, M. Takata, M. Sakata, and K. Kato, *J. Mater. Chem.* **12**, 3733 (2002).
- ²⁶F. J. Humphreys and M. Hatherly, *Recrystallization and Related Annealing Phenomena*, 1st ed. (Pergamon, New York, 1995).
- ²⁷J. Canny, *IEEE Trans. Pattern Anal. Mach. Intell. PAMI-8*(6), 679 (1986).